

## Contributions of the horizontal ocean-bottom node components to P-wave imaging

Samara M. Garvey<sup>1</sup>, Jim Simmons<sup>1</sup>, and Carlos Calderón-Macías<sup>2</sup>

### Abstract

Horizontal (H) components of ocean-bottom node surveys are acquired at no additional cost to the extensively analyzed vertical (Z) and pressure components. Despite this, H components are seldom processed for reflected converted P to S waves (PS waves) and less so for reflected P waves (PP) due to a perceived lack of value relative to the added processing cost. Recent advancements in elastic migration methods have sparked interest in the H components given a clear rationale for enhancing PS imaging and interpretation through joint migration. Conversely, the potential benefits of the PP energy observed on the H components (HPP data) are less understood. We investigate the foundational characteristics of HPP data and its contribution to P-wave imaging using idealized acoustic synthetic data sets, free of PS data and surface-related multiples. HPP illumination varies with respect to bed structure (e.g., dips and depth) similar to traditional Z-component P-wave (ZPP) data but is more sensitive to acquisition geometries. Specifically, we develop observations of polarization and strong illumination biases to signed offsets, which motivate a need for strategic handling of HPP data in processing flows. Using partial-offset stacks, we determine that HPP data enhance traditional ZPP imaging most effectively for shallow dipping beds and beneath salt overhangs where intersalt multiples complicate the ZPP image. Our results elucidate the broader need for studying the sensitivities of all component data prior to joint processing and, more specifically, present new understandings of how HPP data can be optimally used to reduce the uncertainties of traditional ZPP imaging.

### Introduction

Ocean-bottom node (OBN) surveys in offshore exploration, compared with traditional surface streamer surveys, have the operational advantage of allowing for the acquisition of longer offsets and richer azimuth sampling, both of which aid in velocity model building (VMB) and the imaging of complex geologic settings (Mei et al., 2019; Huang et al., 2023). In addition, the advantages of acquiring PS-wave information, dominantly recorded on the horizontal (H) components have played a role in the growing interest in OBN surveys. This is driven by the increased feasibility of elastic propagation in imaging, which requires leveraging the complete wavefield recorded on all components of OBN data. Studying the sensitivity of each component (pressure, vertical [Z], and H) to all wave modes is an important first step in understanding possible advantages or pitfalls in the use of multicomponent (MC) data required for elastic workflows.

H components of OBN surveys are often used in preprocessing procedures, for example, in sensor orientation that uses all components (e.g., Gaiser, 1998;

Dellinger et al., 2002) and in specialized applications such as simultaneous source deblending (Jennings and Ronen, 2017) that use signal polarization as additional statistics for source separation. In terms of interpretation, noteworthy applications of the H components leverage the PS signal where sufficiently recorded in specific geologic conditions. Examples include gas cloud imaging (Nahm and Duhon, 2003), S-wave splitting for fracture characterization (Lou et al., 2001), hydrocarbon validation using joint inversion (e.g., Damasceno et al., 2021; Cafarelli et al., 2006), and S-wave VMB using full-waveform inversion (FWI) (e.g., Vigh et al., 2014; Masmoudi et al., 2021; Eivind Dhelie et al., 2022). In sparse OBN surveys, PS-wave interpretation can be hampered by poor subsurface illumination caused by a coarse sampling of the receivers and potentially lower signal to noise (e.g., Ata et al., 2013; Casasanta and Gray, 2015; Holden et al., 2016).

Reflected P-wave (PP) energy recorded on the H components (HPP data) has been largely overlooked. In addition to the drawbacks associated with sparse acquisition previously mentioned, there are at least two

<sup>1</sup>Colorado School of Mines, Department of Geophysics, Golden, Colorado, USA. E-mail: somar@mines.edu (corresponding author); jsimmons@mines.edu.

<sup>2</sup>TGS, Houston, Texas, USA. E-mail: carlos.calderon@tgs.com.

Manuscript received by the Editor 26 September 2024; revised manuscript received 21 February 2025; published ahead of production 4 May 2025; published online 21 July 2025. This paper appears in *Interpretation*, Vol. 13, No. 3 (August 2025); p. SC45–SC56, 8 FIGS. <https://doi.org/10.1190/INT-2024-0145.1> © 2025 Society of Exploration Geophysicists and American Association of Petroleum Geologists

historical factors that have likely discouraged analyzing HPP data. First is the expectation that the PP signal is dominantly polarized in the Z-direction due to the mostly positive velocity gradient in the subsurface. This hypothesis is possibly valid in flat layered geology but in structurally complex regions, which have historically been surveyed with short offset, narrow azimuth acquisitions, the observed lack of HPP data is likely due to the limited aperture. Zhao (2008) presents several 3C acquisition case studies (albeit on land) where HPP signal can be observed on the H-component shot gathers. We refer the reader specifically to Figures 1 and 8 in Zhao (2008). Similarly, the OBN acquisition presented in the Zhang et al. (2021) field study reveals strong HPP energy on the MC shot gathers. Both field-data publications focus on the value of the PS information recorded on the H components (HPS data) and treat the HPP data as coherent noise. Along this vein, when targeting only the HPP data, the HPS data translate as coherent noise. This is the second factor limiting the exploitation of HPP data, as it is potentially masked

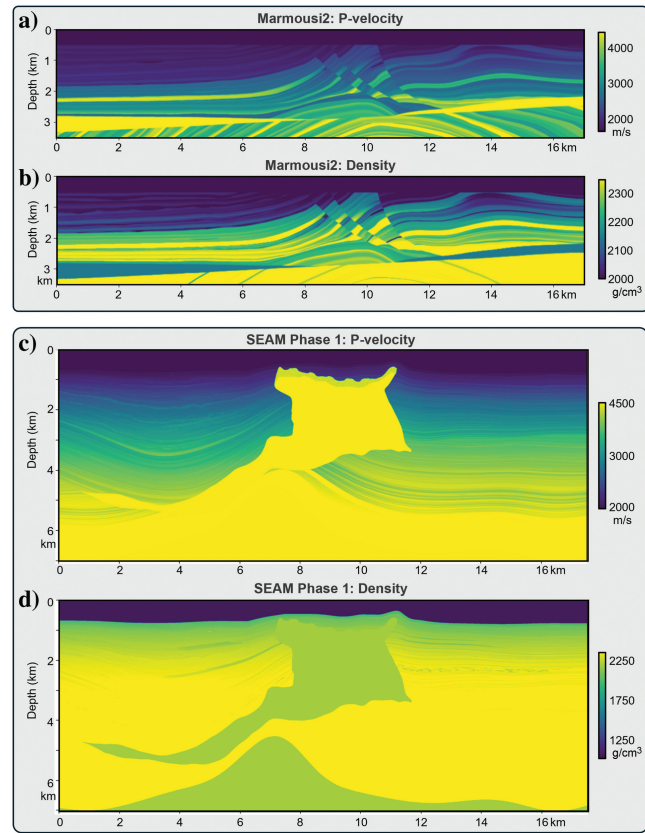


**Figure 1.** The P-wave velocity ( $V_p$ ) and density ( $\rho$ ) models modified from the Marmousi2 data set created by Martin et al. (2002) are depicted in (a) and (b), respectively. Transition layers are removed from the original model, which places the seafloor at a depth of 0.512 km. The 2D P-wave velocity ( $V_p$ ) and density ( $\rho$ ) models extracted from the SEAM Phase 1 data set created by Fehler and Kelihier (2011) are shown in (c) and (d), respectively. Acquisition geometries for the acoustic finite-difference forward modeling of an OBN survey for each model are described in the text.

by the strong PS signal. Despite this, the Liu and Simmons (2024) brief presentation of HPP images generated from an elastic simulation of the SEAM II Barrett model is a motivating example for our investigation. This study is focused on identifying and understanding the distinctive behavior of HPP data, and as such, we strategically do not model the shear modes. Although our preliminary acoustic experiment simplifies MC field data considerably, it effectively characterizes geologic scenarios where integrating HPP data into migration algorithms could yield substantial benefits.

In practice, P-wave imaging procedures may begin with summing the pressure and Z components (i.e., PZ summation) for separating the up- and downgoing energy at the ocean floor (Seher et al., 2022) and for removing S-wave energy (Yang et al., 2020). The downgoing wavefield is particularly beneficial for near-surface imaging when mirror migration methods are implemented (Wang et al., 2010). These PZ summations require assumptions in scaling the energy of the Z-component data, based on the emergence angle, such that the unwanted wave modes cancel out (Soubaras, 1996). Thus, although the pressure component arguably detects P waves from all angles, the downgoing wavefield used in imaging and interpretation emphasizes the events detected on the Z-component. This rationale motivates our experimental decision to not simulate free-surface effects. That is, acknowledging that PZ summation focuses working data sets to P waves on the Z-component (ZPP data), we model the upgoing wavefields and focus our analysis on the Z and H components. It is worth mentioning that given this upgoing-only wavefield simulation, the insights into ZPP versus HPP data presented in this study apply to 3C land data as well.

The paper begins by introducing the 2D synthetic models used to simulate idealized acoustic OBN data sets. The choice of the Kirchhoff prestack depth migration (KPSDM) algorithm for imaging is then justified, with details provided on the parameterization and handling of OBN geometries. Each case study is analyzed individually, with the analysis centering on the use of partial stack images to evaluate the characteristics and contributions of HPP versus ZPP illumination. This is followed by a summary of the generalized characteristics of HPP data, offering new insights into the handling and use of H-component data, which are further discussed before concluding remarks are presented.

## Numerical models and simulations

We simulate OBN acquisitions on two familiar industry models — the shallow water, faulted setting of the 2D Marmousi2 model (Martin et al., 2002) and a 2D section of the deepwater, salt model published by SEG SEAM (Fehler and Kelihier, 2011). The Marmousi2 model is a 17 km  $\times$  3.5 km cross section representative of the North Quenguela Trough in the Cuanza Basin, Angola. The P-wave velocity and density models for this case study are shown in Figure 1a and 1b, respectively. It is an elastic

extension of the acoustic Marmousi model and allows for easy extension of this work with elastic simulations. To simulate a best-case scenario for HPP imaging, the Marmousi2 model was modified to replace the shallow transition layers at the seafloor with a water layer. The ocean-bottom data were thus recorded on the new seafloor at a depth of 0.512 km. The grid and cell sizes of the model are  $4250 \times 875$  and  $4 \text{ m} \times 4 \text{ m}$ , respectively. The SEAM Phase 1 model is analogous to a complex salt domain in the Gulf of Mexico and the extent of the 2D cross section is  $17.5 \text{ km} \times 7 \text{ km}$ . The P-wave velocity and density models for this case study are shown in Figure 1c and 1d, respectively. The grid and cell sizes of the model are  $1751 \times 1401$  and  $10 \text{ m} \times 5 \text{ m}$ , respectively. Compared with the Marmousi2 model, the seafloor depth varies from 500 to 1000 m. OBN geometries for both models were simulated by placing receivers every 25 m at the water-solid interface. Sources were characterized by a symmetric 15 Hz Ricker wavelet and spaced 25 m at a constant depth of 10 m in the water column.

To effectively highlight the kinematics of the HPP data, we forward model the acoustic wave equation without implementing the standard free-surface condition to forestall the generation of PS waves and surface-related multiples. We simultaneously model the pressure, Z-, and H-displacement wavefields by solving a system of two coupled first-order equations, respectively, describing the vector displacement and scalar pressure fields. These equations were iteratively solved using a forward marching, staggered in time finite-difference scheme implemented with the Devito software package (Louboutin et al., 2019; Luporini et al., 2020).

## Coordinate system framework

At any receiver, the detected signal's polarity depends on the coordinate system convention and subsurface properties, i.e., layer geometries and elastic properties. We assume an acquisition coordinate system in which the positive Z- and X-directions point upward and to the right, respectively. Assuming a horizontally layered earth model with OBN acquisition (Figure 2), an upgoing reflected wave is detected as a positive displacement in Z, whereas a downgoing direct wave is detected as a negative displacement in Z. Receivers located to the right of the source are designated as positive-offset receivers, whereas those to the left are considered as negative-offset receivers. For particle motion recorded along the X-direction, positive-offset receivers detect positive displacements in X and negative-offset receivers detect negative displacements. This reversal of horizontal particle motion at zero offset is realized as opposite polarities on the recorded X-component shot gathers and is hereon referred to as a signed-offset polarization bias (SOP bias).

We show an example of the Z- and X-component shot gathers at 3.0 km on the Marmousi2 model (Figure 3a and 3b) where the stratigraphy is relatively flat. All energy observed on these gathers is P wave due to the acoustic forward modeling. For the flat layered stratigraphy at near offsets, this PP energy is dominantly recorded on the Z-component, and at far offsets, the energy is distributed onto the Z and X components. As expected by the coordinate system definition, the direct wave (yellow arrow) is recorded with negative polarity on all offsets of the Z-component gather and the negative offsets of the X-component gather. On the positive offsets of the X-component, this direct wave is recorded with positive polarity. The strong signal at approximately 0.8 s (blue arrows) is a reflected P wave from the top of a gas reservoir and should have a negative amplitude because of the negative impedance contrast. This reflection is recorded as negative polarity on all offsets of the Z-component and on the positive offsets of the X components. On the negative offsets of the X components, the recorded signal has a positive polarity.

The use of a radial-transverse (R-T) horizontal coordinate system successfully removes this SOP bias for reflectors parallel to the recording surface. The R direction for any source-receiver pair points along the source-to-receiver azimuth (Gaiser, 1999). Figure 3c shows the result of this rotation at 3.0 km. The direct wave and reflected gas-pocket signal are detected as positive and negative polarities, respectively, regardless of signed offset. Where subsurface layers are dipping, the conversion to the R-T system imposes an SOP bias. This is observed on the shot gathers at 9.3 km of the Marmousi2 model where the layers are severely tilted and faulted. In Figure 3d–3f, we show the Z, X, and R shot gathers and annotate the X and R components with pink arrows to highlight the SOP observations.

Stacking across signed offsets in either the X- or R-direction can potentially distort or cancel signal

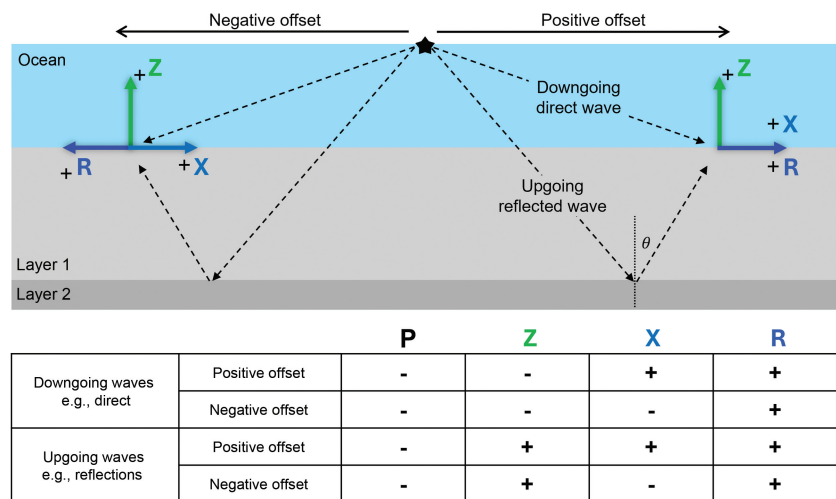


**Figure 2.** Description of coordinate system for OBN acquisition. The table describes the polarity of different waves registered on the positive or negative offsets of the pressure, Z, X, and R components.

depending on the target bed geometry. As rotation to R-T is a standard industry practice, our initial analyses include a cross-examination of the X- and R-component data where the forward-modeled 2D data are rotated to the R direction prior to migration.

### Migration algorithm

The selection of a migration algorithm can be streamlined into choices between ray-based versus wavefield-based and vector-based versus scalar-based migrations. Ray-based migrations such as KPSDM are computationally inexpensive compared with wavefield-based approaches such as reverse time migration (RTM). Furthermore, obtaining “true” relative amplitude gathers is more efficient and straightforward with

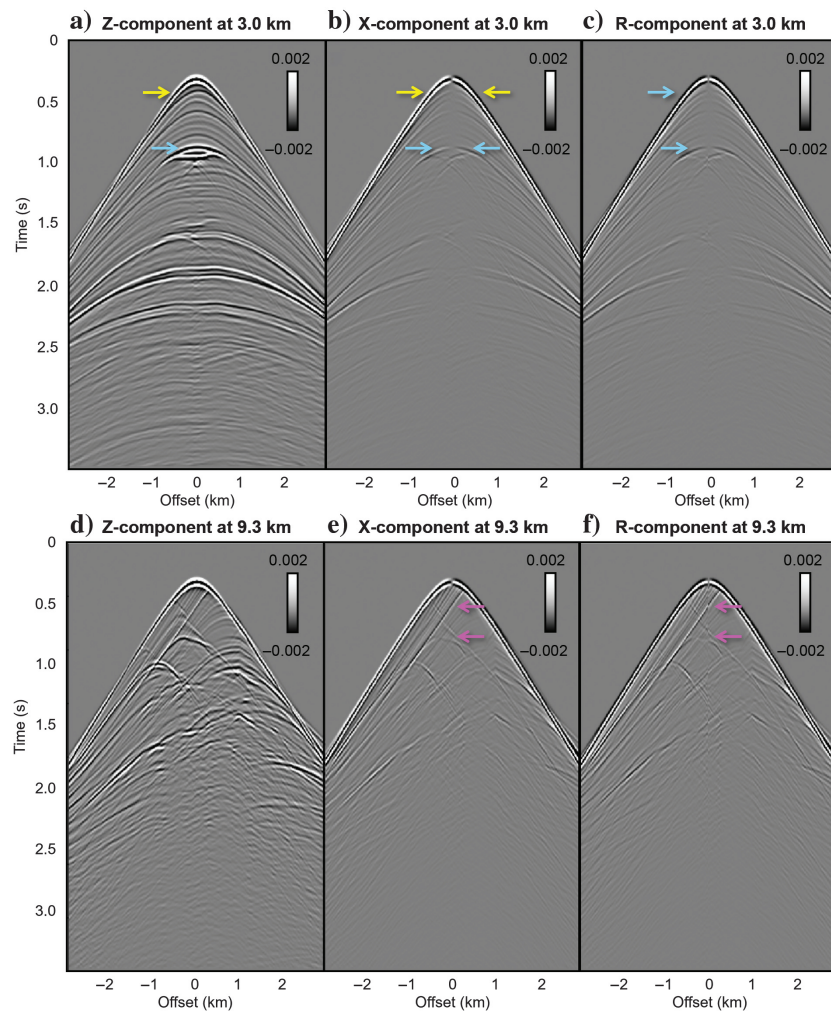


**Figure 3.** Raw shot gathers from the Marmousi2 experiment for the Z, X, and R components at 3.0 km (a–c), where the stratigraphy is relatively flat, and at 9.3 km (d–f), where the beds are severely tilted and faulted. (a–c) Yellow and blue arrows highlight the direct arrival and the reflection at the top of a gas reservoir, respectively, for each component. For direct and reflected waves at this location, we observe uniform polarity at all offsets for the Z-component and an SOP on the X-component, which is corrected by rotation to the R-direction. (e and f) Pink arrows highlight comparative dipping bed reflectors: on the X-component, no SOP is observed, whereas on the R-component, an SOP is introduced due to rotation.

KPSDM compared with RTM. For these trivial reasons, KPSDM remains an industry standard in most geologic regimes or at the very least, used in fast-track processing in regions with complex subsurface structures. Another benefit to ray-based approaches is the ease of migrating distinct wave modes controlled by the input traveltime field estimations, i.e., scalar wavefield migration (Bucha, 2021). Although this distinctive imaging is possible in wavefield-based migrations, the severe crosstalk of unwanted wave modes often require wavefield separation (effectively migrating each wavefield with a scalar algorithm, e.g., Yan and Sava [2009]) or an advanced imaging condition (treating the problem as a vector-based joint migration, e.g., Hou and Marfurt [2002] and Rocha et al. [2016]). Vector-based migrations of elastic data often use the MC data sets and produce separate P- and S-wave images. These vector approaches may be implemented in ray- or wavefield-based migrations (Hokstad, 2000). The interest in vector-based elastic RTMs in structurally complex, marine environments is increasing due to more activity in ocean-bottom surveys, which facilitate PS-wave acquisition. This is motivated by the need for time-lapse studies of reservoir conditions requiring P- and PS-wave information. Although the H components are valued for the PS-wave data in joint processing workflows, it is poorly understood how the HPP data impact vector-based migrations of P-wave data. Thus, we use a scalar-based KPSDM such that the P-wave information on each component was separately imaged and the independent contributions of ZPP versus HPP data can be assessed. We continue the discussion of migration algorithms in the “Discussion and suggestions for further investigation” section considering the results presented.

The specific KPSDM code used (written by Liu [1993] and found in Seismic Unix [SU] [Stockwell, 1999]) is based on the Bleistein et al. (1987) integral formulation, which is kinematically accurate for direct pure-mode and converted-wave modes (Bleistein, 1986). Our analysis emphasizes subsurface reflection point illumination differences of the ZPP and HPP images and not on reflection amplitude differences. All components were migrated with the same ray tracing and migration parameterizations. The code was modified to use two distinct traveltime fields for sources and receivers having different elevation data. This

modification makes the Kirchhoff code directly suitable for ocean-bottom geometries. Source-side and receiver-side traveltime tables for input to the KPSDM were calculated using a 2D paraxial ray-tracing algorithm (Liu, 1993). We performed ray tracing on a smoothed version of the true P-wave velocity models for both case studies. Turning rays were not migrated. Maximum offsets recorded for the Marmousi2 and SEAM Phase 1 models were 3000 and 5000 m, respectively, and a migration aperture equal to these maximum recorded offsets was used for both case. Prior to stacking, data were migrated into common-image gathers (CIGs) at 0.1 km offset bins with a 45° outside mute and mild band-pass filter.

## Results: Marmousi2 case study

The Marmousi2 model provides a convenient opportunity to begin analyzing HPP illumination for flat versus tilted stratigraphy. Figure 4 presents the Z, X, and R CIGs at the two shot gather locations shown in Figure 3a–3c and Figure 3d–3f. At both locations, the migrated PP reflections on the X and R CIGs are flattened similar to that of the Z-component (blue arrows). The SOP bias observed in the X- and R-component shot gathers in Figure 3 persists in the CIGs — at 3.0 km, rotation to R corrects the X-component SOP bias, whereas at 9.3 km, the rotation instead introduces an SOP bias.

A closer examination of the 9.3 km CIGs reveals a signed-offset illumination (SOI) bias on the H components (X and R), which were not immediately obvious on the shot gathers. Specifically, some steeply dipping beds that are uniformly illuminated across all offsets on the Z-component exhibit differences in amplitude and resolution between positive and negative offsets on the X and R components (refer to pink arrows in Figure 4d–4f). This SOI bias, which exists on some reflections regardless of horizontal coordinate system, underscores the importance of understanding how images and interpretations differ between positive- and negative-offset stacks of the H-component data. In the remaining analyses of this work, we focus on the R components for reasons outlined in the “Coordinate system framework” section.

Partial-offset stacks are generated with the following angle ranges: 0°–10° ultranear, 10°–20° near, 20°–30° mid, and 30°–45° far. These angles ( $\theta$  in Figure 2) are computed as the emergent angles assuming flat model layers.

Figure 5 compares partial-offset stacks of the RPP data, specifically ultranear versus mid-offset stacks in the most structurally complex area of the model. At ultranear offsets, dips are similarly illuminated on positive- and negative-offset stacks (Figure 5a and 5b, respectively), whereas at the respective midoffsets (Figure 5c and 5d), the SOI bias is stronger. These observations are annotated with yellow arrows noting that on mid-offset stacks, the left-dipping events are better imaged on the negative-offset stack.

Our analysis of the Marmousi2 synthetic OBN data reveals two key findings about H-component records, independent of the chosen coordinate system: (1) polarization and (2) illumination varies systematically between positive and negative offsets, depending on subsurface geometry. Notably, receivers positioned downdip relative to a given reflector capture stronger HPP energy, highlighting the importance of partial-offset HPP stacks

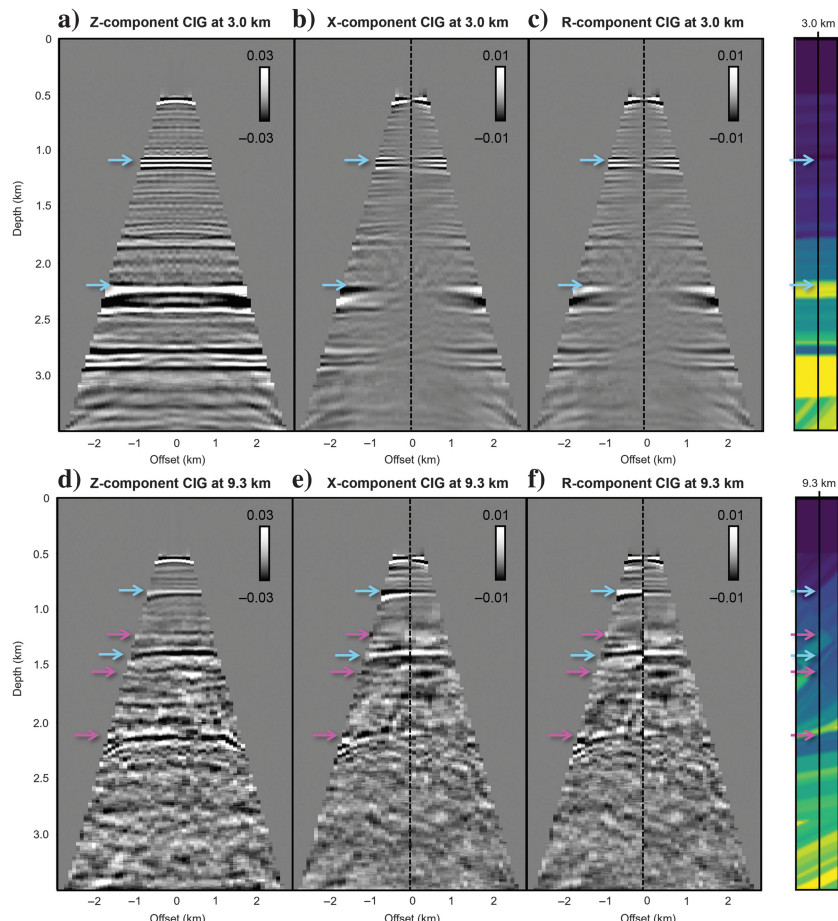


**Figure 4.** The CIGs from the Marmousi2 experiment at shot locations 3.0 km (a–c) where stratigraphy is relatively flat and 9.3 km (d–f) where beds are severely tilted and faulted. The H components (X and R) are gained three times the amplitude of the Z-component and all gathers have an outer mute of 45° applied. Using the same parameterizations for KPSDM, the PP energy on all components is equally flattened (blue arrows) at both locations. Pink arrows on the 9.3 km CIGs highlight dipping bed reflections, which are uniformly illuminated at all offsets on the Z-component, but are illuminated differently between the positive and negative offsets of the X and R components.

when imaging uniform dips. To explore how these data can complement traditional ZPP interpretation, we now turn to a salt imaging study — a common industry challenge in the pursuit of salt-juxtaposed reservoirs.

## Results: SEAM Phase 1 case study

Imaging subsalt and salt flanks in marine environments are often difficult because of sparse illumination. The SEAM example investigates the value of HPP illumination in resolving such subtle salt-edge features using partial-offset images generated using the same angle ranges as in the Marmousi2 example.

Figure 6 compares the full (ultranear to far) signed-offset stacks of the migrated ZPP and RPP data. Although the migration did not incorporate turning ray information necessary for imaging a continuous base of salt, the RPP images show a more focused base of salt reflector wherever it is illuminated in comparison to the corresponding ZPP images (yellow arrow annotations). This is partly attributed to the strong interference of poorly migrated intersalt multiples on the ZPP images (blue arrows in Figure 6a and 6b).

Although some multiples are observed on the RPP images (blue arrows in Figure 6c and 6d), they are relatively weak compared with the primary reflections.

Similar to the Marmousi2 observations, the SOI bias of the RPP data is more pronounced in the RPP data (compare Figure 6c versus 6d) than in the ZPP data (compare Figure 6a versus 6b). We also note that negative-offset RPP data best illuminate left-dipping sediment layers (on the left side of the salt body in Figure 6d) and vice versa for right-dipping sediment layers (on the right side of the salt body in Figure 6c) and that multiple contamination on RPP differs between signed-offset images.

In deepwater settings, prolific hydrocarbon reservoirs are often trapped against salt flanks and beneath salt overhangs. Figure 7 examines the imaging of the right flank with positive, partial-offset stacks (red box 1 in Figure 6a) and Figure 8 examines the left flank with negative, partial-offset stacks (red box 2 in Figure 6a).

The regions where RPP illumination enhances areas of poor ZPP salt flank imaging vary across the data set. For example, the right-dipping salt flank (annotated on

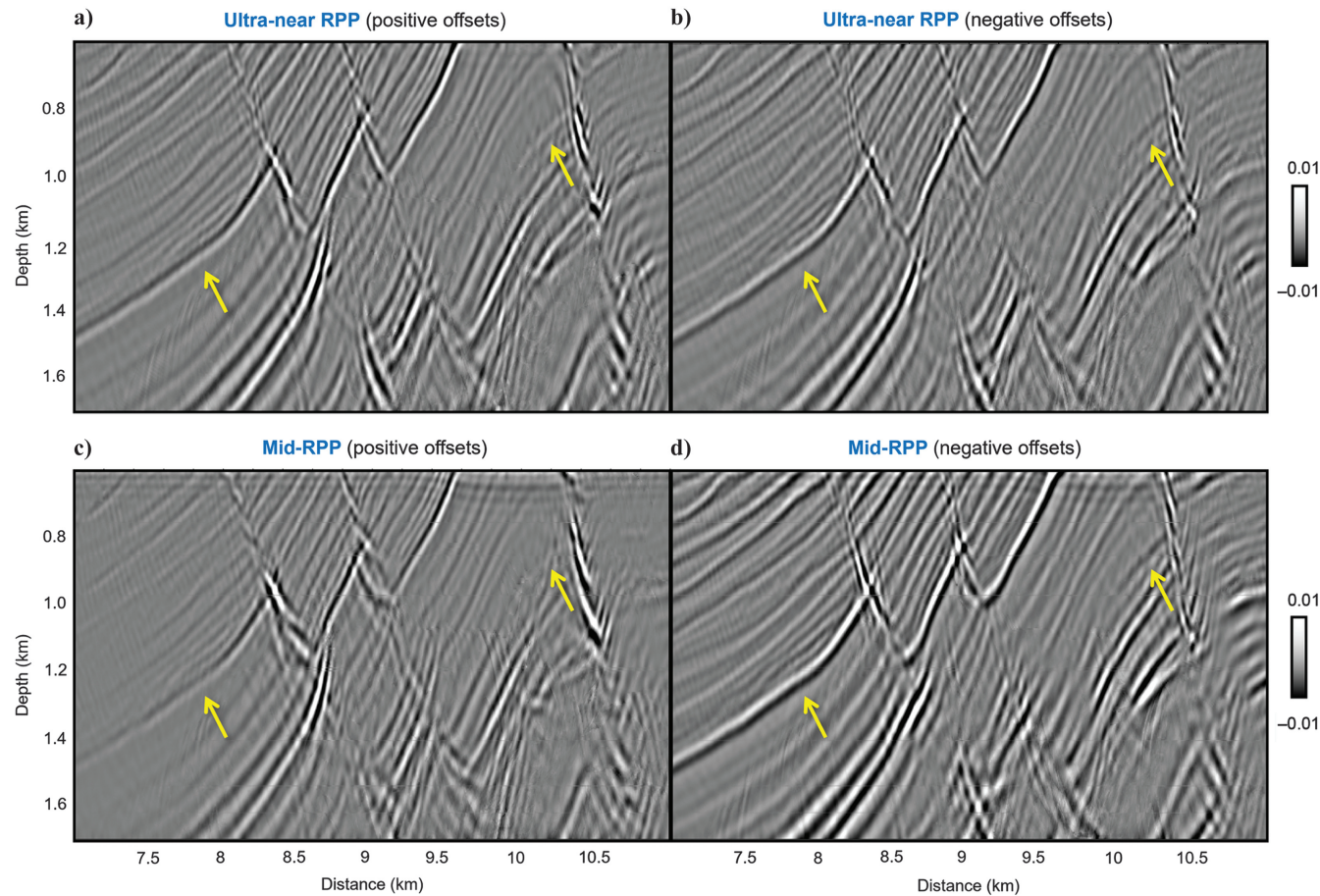


**Figure 5.** Comparison of the RPP (a and b) ultranear and (c and d) mid partial-offset stacks for (a and c) positive and (b and d) negative offsets. All panels are displayed on the same amplitude scale. Yellow arrows highlight left-dipping bed reflections, which are similarly imaged (disregarding polarity) on the ultranear stacks but better imaged on the negative mid-offset stacks as a result of the biased HPP illumination to signed offset.

a few panels in Figure 7 with dotted yellow arrows) is similarly and continuously imaged on all ZPP and RPP partial-offset images; however, the shallow salt edge (solid yellow arrow annotations) benefit more from RPP illumination than ZPP (particularly at mid to far

offsets). In addition, in some instances, the overhang reflector is better focused on the RPP image compared with the corresponding ZPP image. Such examples on Figures 7 and 8 are annotated with blue arrows and, in particular, the continuity of the overhang on the RPP

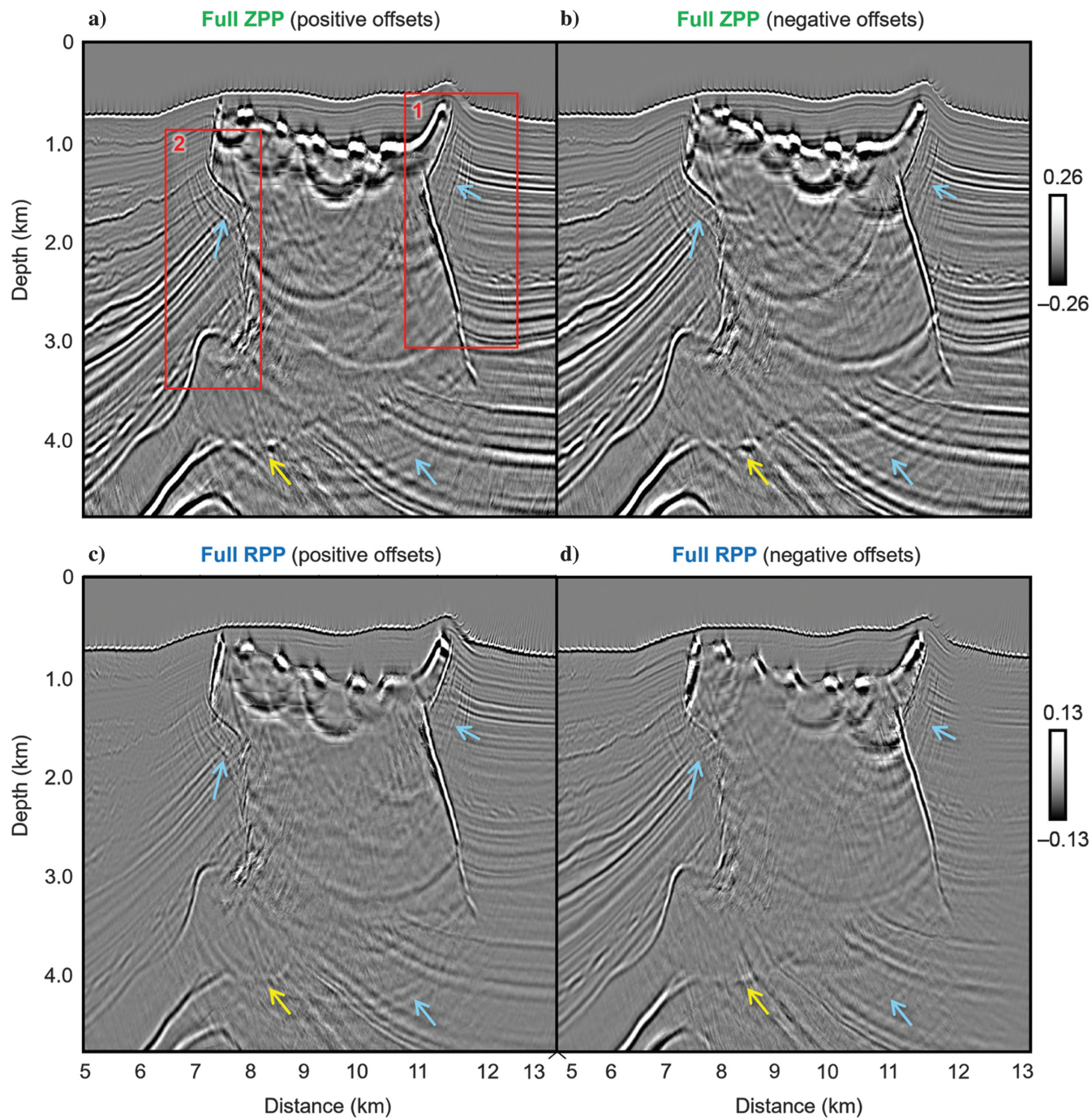


**Figure 6.** Comparison of full ( $0^{\circ}$ – $45^{\circ}$ ), signed-offset stacks for (a and b) ZPP and (c and d) RPP data. RPP images are gained two times the amplitude of the ZPP images. RPP illumination has a stronger SOI bias (compare the differences in [c] and [d]) versus the ZPP illumination (compare the minor differences in [a] and [b]). In general, RPP data supplement the ZPP data in critical locations below the salt overhangs and at the base of salt. Yellow arrows highlight the base of salt illumination, which is more continuous on the RPP images as opposed to the ZPP images, which are more affected by poorly migrated intersalt multiples. Blue arrows highlight these multiples in regions below the salt and under the salt overhangs. Red boxes 1 and 2 on (a) outline the magnified regions shown in Figures 7 and 8, respectively.

image in Figure 8e is a convincing example of the relevance of the RPP illumination to imaging even at near offsets.

Similar to the discontinuous salt flank imaging, the imaging of dipping beds that are weakly illuminated on ZPP can be supplemented by the RPP illumination of these reflectors. Dotted white arrows in Figures 7 and 8 highlight a few such reflectors at all offsets.

Under the salt overhangs, solid white arrows annotate unique observations where the intersalt multiples contaminate the ZPP images more than the RPP data. An additional noteworthy observation is that in some scenarios where these intersalt multiples are recorded on the R-component and they are inverted polarity to the recorded polarity on the Z-component. For example, we compare the highlighted multiple in Figure 7a versus 7e.

Assuming that the SOP biases can be remedied with a vector-based migration, then stacking the ZPP and RPP data can provide several benefits to salt basin imaging, which include improving the illumination of steeply dipping reflectors (such as salt flanks and salt-juxtaposed beds) and suppressing multiple interference under overhangs. Using the ZPP and RPP data potentially improves the resolution of salt-sediment interfaces, which improves the interpretation of potential trapping and sealing mechanisms critical for accurate hydrocarbon prospecting.

### Summary of observations

We observe that the reflected P-wave data recorded on the H-component contains sufficient signal that after migration, illuminates dipping reflectors differently, but complementary, to the Z-component illumination. The strength of the HPP signal is a function of target depth

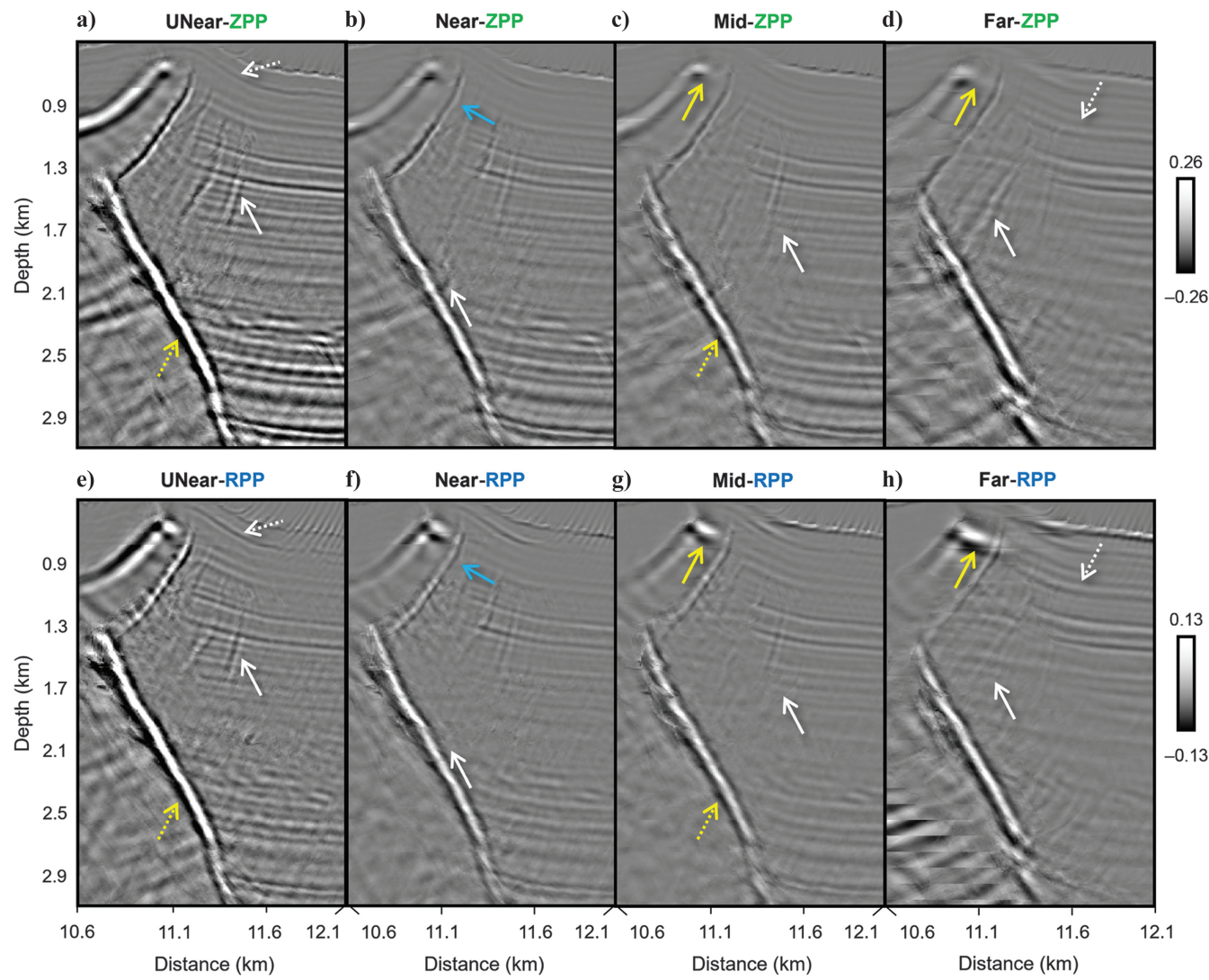


**Figure 7.** Positive partial-offset stacks magnified to the right salt flank of the SEAM Phase 1 model. Magnified region is described in Figure 6. (a-d) The ZPP ultranear, near, mid, and far partial-offset stacks, respectively, and (e-h) the RPP equivalent stacks. In general, dotted arrows highlight reflectors that are comparably imaged on Z and R components, whereas solid arrows highlight examples where the RPP illumination is significantly better. Yellow arrows highlight observations related to salt imaging and white arrows highlight observations related to stratigraphy. Refer to the text for relevant details.

and dip relative to receiver depth and offset. When P-wave signal is strongest on the H-component, it is weakest on the Z-component and there is potential benefit to jointly analyzing or combining both components. From both studies, we generalize the following observations regarding the reflected P waves:

- 1) The RPP polarities of dipping beds are biased to signed offset (SOP bias), i.e., a dipping interface will be detected with opposite polarities on the negative-versus the positive-offset receivers, which leads to potentially destructive inference in stacking across signed offsets.
- 2) The HPP illumination of dipping beds is biased to signed offset (SOI bias) regardless of coordinate system (X or R). More specifically, beds dipping in the source-to-receiver (offset) direction are best illuminated by receivers positioned on the downdip side of the source.

3) The HPP illumination of the subsurface varies with depth and dip of bed (related to the emergence angle of the reflected wave) and absolute source-receiver offset.

- In the simple Marmousi2 study, these relationships are discernible: shallow, dipping beds are best illuminated at near offsets on both signed-offset H components.
- In the complex SEAM Phase 1 salt study, these relationships are less intuitive and the strength of HPP subsalt and salt-flank imaging varies possibly due to velocity complexity.

## Discussion and suggestions for further investigation

Evaluating the sensitivities of the H components to individual wave modes is crucial for the efficient implementation of joint imaging and analysis of MC data.

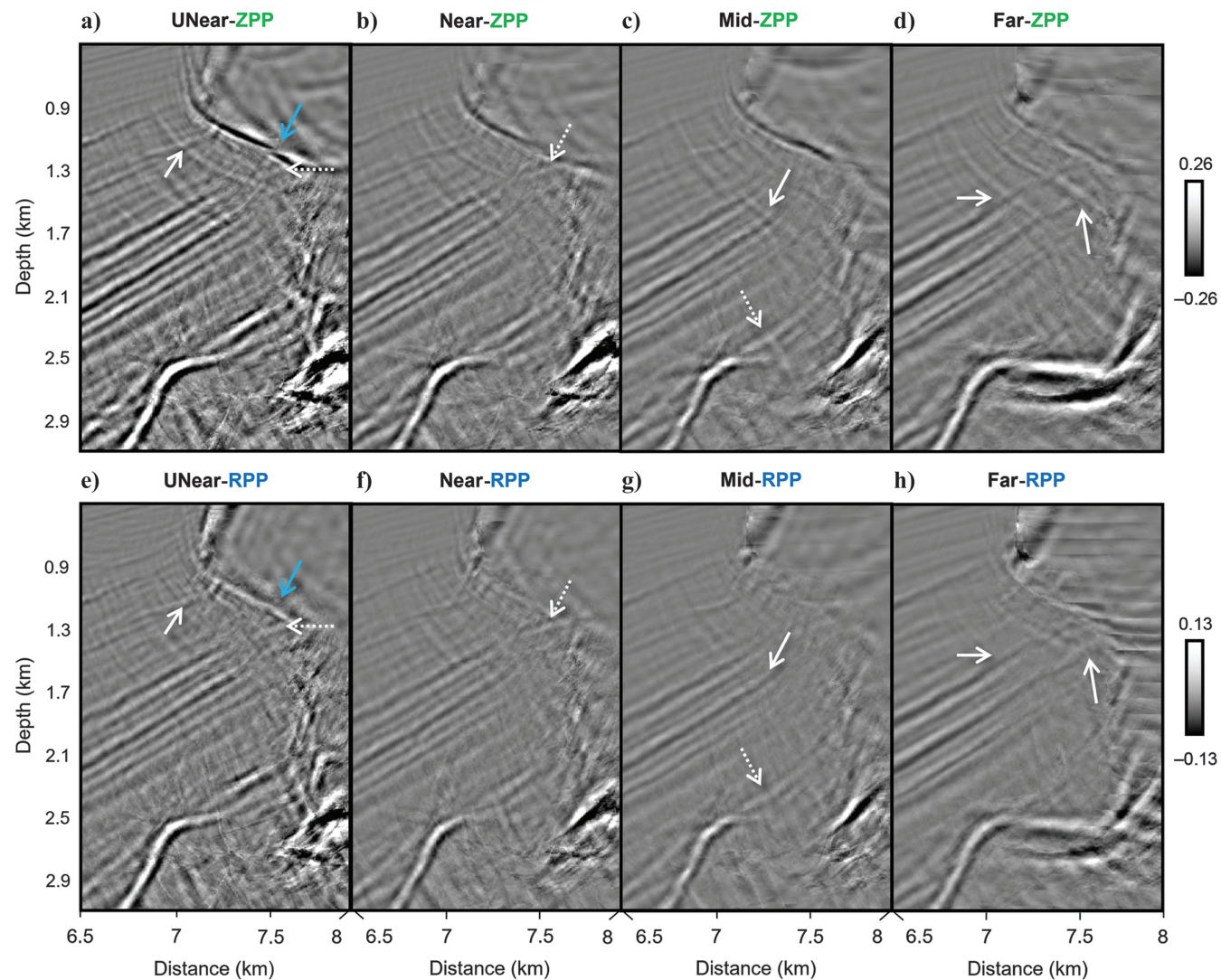


**Figure 8.** Negative partial-offset stacks magnified to the left edge of the main salt body on the SEAM Phase 1 model. Magnified region is described in Figure 6. (a-d) The ZPP ultranear-, near-, mid-, and far-offset stacks, respectively, and (e-h) the RPP equivalent stacks. Descriptions of arrow annotations are the same as those used in Figure 7.

Our synthetic experiments provide evidence of the value of HPP data, even at small offsets, for imaging shallow and/or complex subsurface structures. This has a potential impact not only on resource mapping, e.g., in deep-water salt field or shallow gas hydrate (Backus et al., 2006) exploration but also on shallow hazard mapping for well-planning or other geotechnical seafloor projects.

The choice of acoustic experiments has allowed us to establish a fundamental understanding of HPP data in isolation from other wave modes. Repeating these analyses on elastic data sets or with free-surface effects is natural progressions of this work. Based on our observations of strong biases in HPP illumination toward signed offsets, we anticipate similar biases in the case of free-surface multiples and PS waves in elastic media.

The use of KPSDM in this study presents advantages and limitations. KPSDM is widely used for its efficiency and adaptability; however, its reliance on a ray-based imaging model limits proper migration to only single-point reflection events. In regions with strong velocity contrasts and/or complex 3D structural geology, KPSDM of multiple reflections and refractions can result in artifacts. Although these limitations may introduce uncertainties in the interpretation, they do not diminish the significance of our key observations. The systematic SOP and SOI biases remain fundamental aspects of the recorded HPP wavefield, independent of the imaging method. However, it is possible to resolve these biases by accounting for the direction of emerging particle motion relative to the receiver directions. Exploring such imaging methods could help assess the robustness of these findings.

Correcting the SOP concerns (associated with item A in the summarized observations) would allow for comparison of amplitudes in the ZPP and HPP images. This has been discussed and exemplified in Kirchhoff migration applications of 3D VSP data (Dillon, 1990; Gherasim et al., 2005) and multichannel teleseismic receiver functions (Bostock, 2002; Millet et al., 2019). Implementation of vector-based migrations such as the vectorial-based Kirchhoff migrations as presented by Kuo and Dai (1984) or RTM using the energy-norm imaging condition by Rocha et al. (2016) also can account for these amplitude variations with emergence angle. A comparison of these vector-based migrations on separated signed-offset data has the potential to produce better images by capitalizing on the signed-offset biases of the HPP data.

Regarding multiples, our results have demonstrated weaker interbed salt multiples on HPP compared with ZPP. Thus, it is important that these strong ZPP multiples are sufficiently attenuated prior to joint migration; otherwise, the contributions of the HPP data in critical regions, such as under salt overhangs and along flanks, may be masked by the crosstalk related to these coherent noise events. In instances where interbed multiples are discernible on RPP data, there is potential to leverage the observation of opposite polarities between ZPP and RPP to identify and suppress these undesirable

modes. We hypothesize that surface-related multiples also would weakly impact HPP data, as they tend to propagate more vertically. Where such multiples are recorded on the HPP data, there may be an opportunity to perform a summation of pressure, Z-, and H-component data to achieve a more accurate wave mode separation, which requires estimations of emergence angles (Schalkwijk et al., 2003).

For VMB, although not in the scope of this work, it is apparent from the results presented that using reflected P-wave energy captured in the H-component could benefit the P-wave VMB particularly for shallow geology. Solano and Plessix (2023) demonstrate the value of a joint elastic FWI (EFWI) using the Z and pressure components versus individual inversions of either component. Although the pressure component is omnidirectional, the joint inversion benefits from the S/N of the unidirectional Z-component P-wave records. The higher S/N reflected P-wave signal from the H-component can similarly benefit EFWI workflows. Another plausible method to improve VMB is including the residual moveout picks of the P-signal from the HPP migrated gathers to the conventional picks from the Z-component. With no considerable cost, this potentially improves P-wave model updating without the need for addressing noise in the prestack data before migration. Cho et al. (2022) address the utility of the H-component for the shallow shear VMB in salt fields of the Gulf of Mexico. A potential research opportunity following from our results is investigating the PS-signal recorded on the Z-component and exploring its value to shallow shear VMB, which suffers from sparse receiver acquisition.

## Conclusion

P-wave energy measured on H components has been mostly neglected in MC surveys. We analyze these HPP data for image improvements evidenced by enhanced focusing and continuity of reflectors versus using a single Z-component data set. Using “best-case” acoustic simulations of OBN acquisitions on widely used industry marine models, we demonstrate the added value of HPP illumination, particularly for imaging shallow and dipping subsurface geometries. We make critical observations about SOP and illumination biases in HPP data compared with ZPP data, with these effects becoming more pronounced at steeper dips and shallower depths. HPP images complement and reduce the uncertainty of the ZPP interpretation of shallow, steeply dipping beds or salt flanks, and intriguingly in regions below salt overhangs where inter-salt multiples complicate the ZPP image. Results shown have potential implications for model building methods and in particular for the incorporation of components in tomography and FWI approaches. Including free-surface multiples and converted waves in more complex simulations is a necessary succession of this research, which will address the complexities in MC imaging of field data.

## Acknowledgments

We would like to thank the sponsors of the Reservoir Characterization Project for their financial support and fruitful discussions. We extend our sincere thanks to our reviewers, including Gaiser and Liu, for their insightful feedback and constructive comments.

## Data availability statement

The open-source tools Devito (for forward modeling) and SU (for data processing and migration) can be accessed at their respective websites: <https://www.devito-project.org> and <https://wiki.seismic-unix.org/start>. In addition, the synthetic models used in this study are publicly accessible. The Marmousi2 model is hosted at [https://wiki.seg.org/wiki/AGL\\_Elastic\\_Marmousi](https://wiki.seg.org/wiki/AGL_Elastic_Marmousi), whereas the SEAM Phase1 model is available at <https://seg.org/seam/open-data>. For the simulated OBN data and processing scripts, interested parties can request access from the corresponding author.

## Conflict of interest

The authors declare that there is no conflict of interest regarding the publication of this paper.

## References

Ata, E., R. Olson, C. C. Mosher, S. Shaw, and S. Betterly, 2013, A look at converted waves from an OBN test survey: 83rd Annual International Meeting, SEG, Expanded Abstracts, 5170–5174, doi: [10.1190/segam2013-1477.1](https://doi.org/10.1190/segam2013-1477.1).

Backus, M. M., P. E. Murray, B. A. Hardage, and R. J. Graebner, 2006, High-resolution multicomponent seismic imaging of deepwater gas-hydrate systems: *The Leading Edge*, **25**, 578–596, doi: [10.1190/1.2202662](https://doi.org/10.1190/1.2202662).

Bleistein, N., 1986, Two-and-one-half dimensional in-plane wave propagation: *Geophysical Prospecting*, **34**, 686–703, doi: [10.1111/j.1365-2478.1986.tb00488.x](https://doi.org/10.1111/j.1365-2478.1986.tb00488.x).

Bleistein, N., J. K. Cohen, and F. G. Hagin, 1987, Two and one-half dimensional Born inversion with an arbitrary reference: *Geophysics*, **52**, 26–36, doi: [10.1190/1.1442238](https://doi.org/10.1190/1.1442238).

Bostock, M., 2002, Kirchhoff-approximate inversion of teleseismic wavefields: *Geophysical Journal International*, **149**, 787–795, doi: [10.1046/j.1365-246X.2002.01687.x](https://doi.org/10.1046/j.1365-246X.2002.01687.x).

Bucha, V., 2021, Kirchhoff pre-stack depth scalar migration in a simple triclinic velocity model for three-component P, S1, S2 and converted waves: *Geophysical Prospecting*, **69**, 269–288, doi: [10.1111/1365-2478.13051](https://doi.org/10.1111/1365-2478.13051).

Cafarelli, B., S. Randazzo, S. Campbell, J. F. F. Sobreira, M. A. G. Guimaraes, C. Rodriguez, P. Johann, and C. Theodoro, 2006, Ultra-deepwater 4-C offshore Brazil: *The Leading Edge*, **25**, 474–477, doi: [10.1190/1.2193223](https://doi.org/10.1190/1.2193223).

Casasanta, L., and S. H. Gray, 2015, PS imaging of ocean-bottom data: *The Leading Edge*, **34**, 414–420, doi: [10.1190/tle34040414.1](https://doi.org/10.1190/tle34040414.1).

Cho, Y., C. Pérez Solano, J. Kimbro, Y. Yang, R.-E. Plessix, and K. Matson, 2022, Influence of shear velocity on elastic full-waveform inversion: Gulf of Mexico case study using multicomponent ocean-bottom node data: *Geophysics*, **87**, no. 5, R391–R400, doi: [10.1190/geo2022-0014.1](https://doi.org/10.1190/geo2022-0014.1).

Damasceno, A., A. Tura, and J. Simmons, 2021, The added value of joint PP-PS inversion for reservoir characterization: A case study using Jubarte PRM seismic data (offshore Brazil): *Geophysical Prospecting*, **70**, 121–134, doi: [10.1111/1365-2478.13145](https://doi.org/10.1111/1365-2478.13145).

Dellinger, J., R. Clarke, and P. Gutowski, 2002, Three-dimensional vector infidelity correction by general linear transform: 64th Annual International Conference and Exhibition, EAGE, Extended Abstracts, doi: [10.3997/2214-4609-pdb.5.E005](https://doi.org/10.3997/2214-4609-pdb.5.E005).

Dillon, P. B., 1990, A comparison between Kirchhoff and GRT migration on VSP data: *Geophysical Prospecting*, **38**, 757–777, doi: [10.1111/j.1365-2478.1990.tb01873.x](https://doi.org/10.1111/j.1365-2478.1990.tb01873.x).

Eivind Dhelie, P., V. Danielsen, J. Andre Haugen, E. Davenne, K. Richard Straith, A. Roodaki, M. Peiro, A. Fotsoh, W. Gao, N. Masmoudi, and A. Ratcliffe, 2022, High-resolution FWI of converted-wave data — A case study from the Edvard Grieg field: Second International Meeting for Applied Geoscience & Energy, SEG, Expanded Abstracts, 792–796, doi: [10.1190/image2022-3750679.1](https://doi.org/10.1190/image2022-3750679.1).

Fehler, M., and P. J. Keliher, 2011, SEAM Phase 1: Challenges of subsalt imaging in tertiary basins, with emphasis on deepwater Gulf of Mexico: SEG.

Gaiser, J., 1999, Applications for vector coordinate systems of 3-D converted-wave data: *The Leading Edge*, **18**, 1290–1300, doi: [10.1190/1.1438202](https://doi.org/10.1190/1.1438202).

Gaiser, J. E., 1998, Compensating OBC data for variations in geophone coupling: 68th Annual International Meeting, SEG, Expanded Abstracts, 1429–1432, doi: [10.1190/1.1820176](https://doi.org/10.1190/1.1820176).

Gherasim, M., C. Hoelting, and K. Marfurt, 2005, 3-D VSP elastic Kirchhoff pre-stack depth migration — Vinton Dome, Louisiana: 75th Annual International Meeting, SEG, Expanded Abstracts, 2649–2652, doi: [10.1190/1.2148269](https://doi.org/10.1190/1.2148269).

Hokstad, K., 2000, Multicomponent Kirchhoff migration: *Geophysics*, **65**, 861–873, doi: [10.1190/1.1444783](https://doi.org/10.1190/1.1444783).

Holden, J., D. Fritz, O. Bukola, J. McLeman, R. Refaat, C. Page, J. Brunelliere, S. Sioni, A. Mitra, and X. Lu, 2016, Sparse nodes and shallow water — PS imaging challenges on the Alwyn north field: 78th Annual International Conference and Exhibition, EAGE, Extended Abstracts, doi: [10.3997/2214-4609.201600616](https://doi.org/10.3997/2214-4609.201600616).

Hou, A., and K. J. Marfurt, 2002, Multicomponent prestack depth migration by scalar wavefield extrapolation: *Geophysics*, **67**, 1886–1894, doi: [10.1190/1.1527088](https://doi.org/10.1190/1.1527088).

Huang, H., T. Wang, and J. Cheng, 2023, PS-wave separation of multicomponent seismic data at the land surface based on deep learning: *Geophysics*, **88**, no. 3, V233–V247, doi: [10.1190/geo2022-0282.1](https://doi.org/10.1190/geo2022-0282.1).

Jennings, J., and S. Ronen, 2017, Simultaneous source deblending with the radiality and source-similarity attributes: 87th Annual International Meeting, SEG, Expanded Abstracts, 4909–4913, doi: [10.1190/segam2017-17736410.1](https://doi.org/10.1190/segam2017-17736410.1).

Kuo, J. T., and T.-F. Dai, 1984, Kirchhoff elastic wave migration for the case noncoincident source and receiver: *Geophysics*, **49**, 1223–1238, doi: [10.1190/1.1441751](https://doi.org/10.1190/1.1441751).

Liu, Y., and J. Simmons, 2024, Depth imaging of multi-component seismic data through the application of 2D full-waveform inversion to P-and SH-wave data: SEAM II Barrett model study: *Geophysical Prospecting*, **73**, 795–811, doi: [10.1111/1365-2478.13533](https://doi.org/10.1111/1365-2478.13533).

Liu, Z., 1993, A Kirchhoff approach to seismic modeling and prestack depth migration: 63rd Annual International Meeting, SEG, Expanded Abstracts, 888–891, doi: [10.1190/1.1822645](https://doi.org/10.1190/1.1822645).

Lou, M., Y. Zhang, and L. D. Pham, 2001, Shear-wave splitting and fracture orientation analysis from PS waves — Examples from synthetic and field OBC data: 71st Annual International Meeting, SEG, Expanded Abstracts, 94–97, doi: [10.1190/1.1816796](https://doi.org/10.1190/1.1816796).

Louboutin, M., M. Lange, F. Luporini, N. Kukreja, P. A. Witte, F. J. Herrmann, P. Velesko, and G. J. Gorman, 2019, Devito (v3.1.0): An embedded domain-specific language for finite differences and geophysical exploration: *Geoscientific Model Development*, **12**, 1165–1187, doi: [10.5194/gmd-12-1165-2019](https://doi.org/10.5194/gmd-12-1165-2019).

Luporini, F., M. Louboutin, M. Lange, N. Kukreja, P. Witte, J. Hückelheim, C. Yount, P. H. J. Kelly, F. J. Herrmann, and G. J. Gorman, 2020, Architecture and performance of Devito, a system for automated stencil computation: *ACM Transactions on Mathematical Software*, **46**, 1–28, doi: [10.1145/3374916](https://doi.org/10.1145/3374916).

Martin, G. S., S. Larsen, and K. Marfurt, 2002, Marmousi-2: An updated model for the investigation of AVO in structurally complex areas: 72nd Annual International Meeting, SEG, Expanded Abstracts, 1979–1982, doi: [10.1190/1.1817083](https://doi.org/10.1190/1.1817083).

Masmoudi, N., A. Ratcliffe, M. Wang, Y. Xie, and T. Wang, 2021, A practical implementation of converted-wave reflection full-waveform inversion: 83rd Annual International Conference and Exhibition, EAGE, Extended Abstracts, doi: [10.3997/2214-4609.202112751](https://doi.org/10.3997/2214-4609.202112751).

Mei, J., Z. Zhang, F. Lin, R. Huang, P. Wang, and C. Mifflin, 2019, Sparse nodes for velocity: Learnings from Atlantis OBN full-waveform inversion test: 89th Annual International Meeting, SEG, Expanded Abstracts, 167–171, doi: [10.1190/segam2019-3215208.1](https://doi.org/10.1190/segam2019-3215208.1).

Millet, F., T. Bodin, and S. Rondenay, 2019, Multimode 3-D Kirchhoff migration of receiver functions at continental scale: *Journal of Geophysical Research: Solid Earth*, **124**, 8953–8980, doi: [10.1029/2018JB017288](https://doi.org/10.1029/2018JB017288).

Nahm, J. W., and M. P. Duhon, 2003, Interpretation and practical applications of 4C-3D seismic data, east Cameron gas fields, Gulf of Mexico: *The Leading Edge*, **22**, 300–309, doi: [10.1190/1.1572082](https://doi.org/10.1190/1.1572082).

Rocha, D., N. Tanushev, and P. Sava, 2016, Acoustic wavefield imaging using the energy norm: *Geophysics*, **81**, no. 4, S151–S163, doi: [10.1190/geo2015-0486.1](https://doi.org/10.1190/geo2015-0486.1).

Schalkwijk, K. M., C. P. A. Wapenaar, and D. J. Verschuur, 2003, Adaptive decomposition of multicomponent ocean-bottom seismic data into downgoing and upgoing P- and S-waves: *Geophysics*, **68**, 1091–1102, doi: [10.1190/1.1581081](https://doi.org/10.1190/1.1581081).

Seher, T., H. Masoomzadeh, Y. Ren, S. Baldock, and B. Wang, 2022, Deconvolution of upgoing and downgoing wavefields: A data example from the Noaka OBN experiment: Second International Meeting for Applied Geoscience & Energy, SEG, Expanded Abstracts, 2807–2811, doi: [10.1190/image2022-3744979.1](https://doi.org/10.1190/image2022-3744979.1).

Solano, C. P., and R. Plessix, 2023, Can elastic waveform inversion benefit from inverting multicomponent data? *The Leading Edge*, **42**, 184–189, doi: [10.1190/tle42030184.1](https://doi.org/10.1190/tle42030184.1).

Soubaras, R., 1996, Ocean bottom hydrophone and geophone processing: 66th Annual International Meeting, SEG, Expanded Abstracts, 24–27, doi: [10.1190/1.1826611](https://doi.org/10.1190/1.1826611).

Stockwell, J. W., Jr., 1999, The CPW/SU: Seismic unix package: *Computers & Geosciences*, **25**, 415–419, doi: [10.1016/S0098-3004\(98\)00145-9](https://doi.org/10.1016/S0098-3004(98)00145-9).

Vigh, D., K. Jiao, D. Watts, and D. Sun, 2014, Elastic full-waveform inversion application using multicomponent measurements of seismic data collection: *Geophysics*, **79**, no. 2, R63–R77, doi: [10.1190/geo2013-0055.1](https://doi.org/10.1190/geo2013-0055.1).

Wang, Y., R. Bale, S. Grion, and J. Holden, 2010, The ups and downs of ocean-bottom seismic processing: Applications of wavefield separation and up-down deconvolution: *The Leading Edge*, **29**, 1258–1265, doi: [10.1190/1.3496916](https://doi.org/10.1190/1.3496916).

Yan, J., and P. Sava, 2009, Elastic wave-mode separation for VTI media: *Geophysics*, **74**, no. 5, WB19–WB32, doi: [10.1190/1.3184014](https://doi.org/10.1190/1.3184014).

Yang, C., Y. Huang, Z. Liu, J. Sheng, and E. Camarda, 2020, Shear wave noise attenuation and wavefield separation in curvelet domain: 90th Annual International Meeting, SEG, Expanded Abstracts, 1805–1809, doi: [10.1190/segam2020-3426418.1](https://doi.org/10.1190/segam2020-3426418.1).

Zhang, D., C. Tsingas, A. A. Ghamdi, M. Huang, W. Jeong, K. K. Sliz, S. M. Aldeghaither, and S. A. Zahrani, 2021, A review of OBN processing: Challenges and solutions: *Journal of Geophysics and Engineering*, **18**, 492–502, doi: [10.1093/jge/gxab024](https://doi.org/10.1093/jge/gxab024).

Zhao, B., 2008, Application of multi-component seismic exploration in the exploration and production of lithologic gas reservoirs: *Petroleum Exploration and Development*, **35**, 397–412, doi: [10.1016/S1876-3804\(08\)60088-9](https://doi.org/10.1016/S1876-3804(08)60088-9).

---

Biographies and photographs of authors are not available.